arXiv:2111.07418v1 [cs.CV] 14 Nov 2021

TANDEM: Tracking and Dense Mapping in Real-time using Deep Multi-view Stereo

Lukas Koestler[1*] **Nan Yang**[1,2*,†] **Niclas Zeller**[2,3] **Daniel Cremers**[1,2]

[*]equal contribution [†]corresponding author

[1]Technical University of Munich [2]Artisense
[3]Karlsruhe University of Applied Sciences

Abstract: In this paper, we present TANDEM, a real-time monocular tracking and dense mapping framework. For pose estimation, TANDEM performs photometric bundle adjustment based on a sliding window of keyframes. To increase the robustness, we propose a novel tracking front-end that performs dense direct image alignment using depth maps rendered from a global model that is built incrementally from dense depth predictions. To predict the dense depth maps, we propose Cascade View-Aggregation MVSNet (CVA-MVSNet) that utilizes the entire active keyframe window by hierarchically constructing 3D cost volumes with adaptive view aggregation to balance the different stereo baselines between the keyframes. Finally, the predicted depth maps are fused into a consistent global map represented as a truncated signed distance function (TSDF) voxel grid. Our experimental results show that TANDEM outperforms other state-of-the-art traditional and learning-based monocular visual odometry (VO) methods in terms of camera tracking. Moreover, TANDEM shows state-of-the-art real-time 3D reconstruction performance. Webpage: https://go.vision.in.tum.de/tandem

Keywords: SLAM, Dense Mapping, Multi-view Stereo, Deep Learning

1 Introduction

Real-time dense 3D mapping is one of the major challenges in computer vision and robotics. This problem, known as dense SLAM, includes both estimating the 6DoF pose of a sensor and a dense reconstruction of the surroundings. While there exist numerous well-working and robust RGB-D mapping solutions [1, 2, 3], real-time dense reconstruction from monocular cameras is a significantly more difficult challenge as depth values cannot be simply read out from the sensor and fused. Nevertheless, it is a very important problem, as monocular approaches offer significant advantages over RGB-D-based methods [1] which are usually limited to indoor environment due to the near-range sensing or LiDAR-based [4] solutions which are expensive and heavyweight.

Several deep neural network (DNN) based approaches have been proposed to tackle the problem of monocular tracking and dense mapping by utilizing monocular depth estimation [5], variational auto-encoders [6, 7, 8], or end-to-end neural networks [9, 10]. Unlike the aforementioned works, in this paper, we propose a novel monocular dense SLAM method, TANDEM, which, for the first time, integrates learning-based multi-view stereo (MVS) into a traditional optimization-based VO. This novel design of dense SLAM shows state-of-the-art tracking and dense reconstruction accuracy as well as strong generalization capability on challenging real-world datasets with the model trained only on synthetic data. Figure 1 shows the 3D reconstructions delivered by TANDEM on unseen sequences.

Our contributions. **(1)** a novel real-time monocular dense SLAM framework that seamlessly couples classical direct VO and learning-based MVS reconstruction; **(2)** to our knowledge, the first monocular dense tracking front-end that utilizes depth rendered from a global TSDF model; **(3)** a novel MVS network, CVA-MVSNet, which is able to leverage the entire keyframe window by utilizing view aggregation and multi-stage depth prediction; **(4)** state-of-the-art tracking and reconstruction results on both synthetic and real-world data.

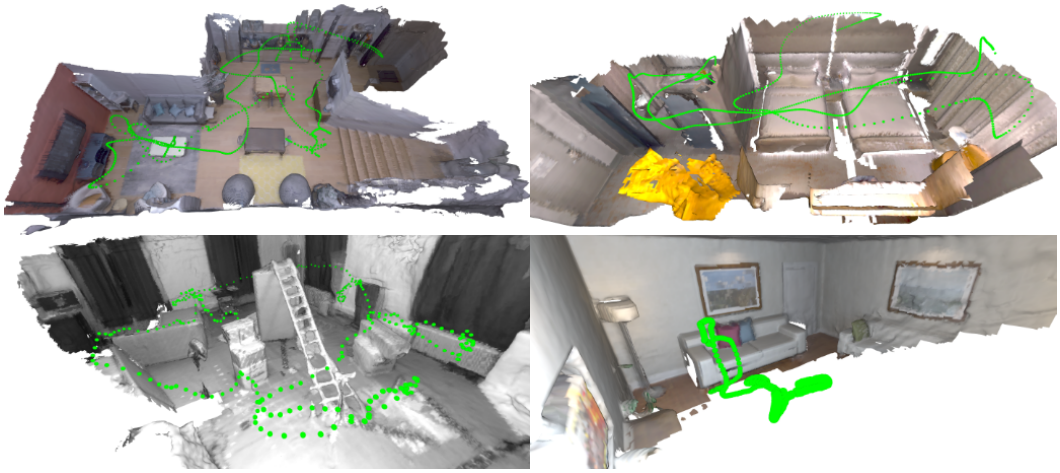

Figure 1: TANDEM is a monocular dense SLAM method that estimates the camera poses and reconstructs the 3D environment in real-time. The figure shows the estimated camera trajectories and the dense 3D models on the sequences of our Replica [11] test split (UL, UR), EuRoC [12] (BL), and ICL-NUIM [13] (BR) using a model trained on the synthetic Replica dataset.

2 Related Work

There are two different work streams related to the proposed method. On one side, there is pure 3D reconstruction based on posed images and, on the other side, there are full SLAM or VO frameworks that simultaneously estimate camera poses and a 3D reconstruction of the environment.

3D Reconstruction. Most dense 3D reconstruction approaches consider images and corresponding reference poses as inputs and estimate a dense or partially dense reconstruction of the environment. Over the last decade, several classical methods have been proposed [14, 15, 16].

Recently, deep-learning-based methods have shown superior performance over classical methods. These methods regress a 3D model of the environment utilizing DNNs. This 3D model can be either in the form of a volumetric representation [9, 17, 18, 19], a 3D point cloud [20] or a set of depth maps [21, 22, 23, 24]. Nowadays, most popular are methods which predict the final model from 3D cost volumes. Huang et al. [21] proposed one of the first cost-volume-based approaches. Zhou et al. [23] aggregate multiple image-pair-wise volumes to a single cost volume and use a 3D CNN for depth prediction. Yao et al. [22] propose to directly calculate a single volume based on 2D deep feature maps predicted from the input images. In a follow-up work, Yao et al. [25] replace the depth prediction CNN by a recurrent network. To improve run-time and memory consumption, Gu et al. [26] propose a cascade cost volume. Yi et al. [27] introduce a self-adaptive view aggregation to weigh the voxel-wise contribution for each input image. The proposed CVA-MVSNet is built upon the two aforementioned works [26, 27] and largely inspired by them. However, only by their combination and adaption to the SLAM setting we achieve better performance and real-time capability.

While all previous methods are based on a set of selected frames, Murez et al. [9] instead directly predict a TSDF model from a single global 3D cost volume. Weder et al. [17] propose a learning-based alternative to classical TSDF fusion of depth maps. While these volumetric representations, in general, are rather memory intense, Niessner et al. [28] propose voxel-hashing to overcome this limitation and Steinbrücker et al. [29] perform depth map fusion on a CPU using an octree.

RGB-D SLAM. In the area of visual SLAM, RGB-D approaches by nature provide dense depth maps along with the camera trajectory and therefore target to solve a similar problem as our approach. Bylow et al. [30] and Kerl et al. [2, 31] mainly focus on accurate trajectory estimation from RGB-D images. In addition to camera tracking, Newcombe et al. [1] integrate the depth maps into a global TSDF representation. Whelan et al. [3] perform surfel-based fusion and non-rigid surface deformation for globally consistent reconstruction. Kähler et al. [32] use a TSDF map representation which is split into sub maps to model loop closures. While most previous methods optimize only for the frame pose, Schöps et al. [33] propose a full bundle adjustment based direct RGB-D SLAM

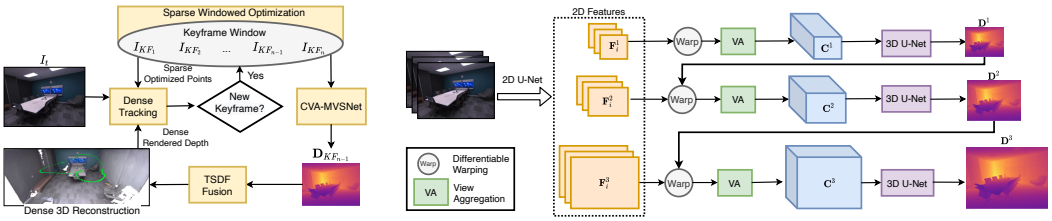

(a) TANDEM System Overview. (b) CVA-MVSNet Architecture.

Figure 2: (a) Every new frame is tracked using the optimized sparse points from the visual odometry and the dense depth map rendered from the 3D model. The poses of the keyframes are estimated by sliding-window photometric bundle adjustment and fed into the CVA-MVSNet for dense depth prediction. The depth maps are fused into a globally consistent TSDF volume. (b) CVA-MVSNet builds cascaded cost volumes and hierarchically estimates the depth maps. The view aggregation module effectively aggregates the features of the multi-view images by predicting self-adaptive weights.

which optimizes for both camera pose and 3D structure. Sucar et al. [34] integrate a DNN-based implicit scene representation into an RGB-D SLAM system.

Monocular SLAM. Compared to RGB-D methods, for monocular approaches both tracking and mapping become much more challenging. Using a single monocular camera, Newcombe et al. [35] perform optimization based on a photometric cost volume to jointly estimate the camera pose and dense depth maps in real-time on a GPU. Pizzoli et al. [36] combine a depth Bayesian filter [37] with the spatial smoothness prior. Engel et al. [38] propose the first large-scale photometric SLAM formulation including loop closure detection and pose graph optimization. By using a sparse representation, Engel et al. [39] were able to formulate the first fully photometric VO framework which jointly estimates pose and depth in real-time. To obtain denser reconstructions, Mur-Artal et al. [40] perform semi-dense probabilistic depth estimation on top of feature-based SLAM [41]. Schöps et al. [42] perform temporal, plane-sweep-based depth estimation using the poses and images obtained from a mobile tracking device. Tateno et al. [5] and Yang et al. [43, 44] leverage DNNs in a traditional direct SLAM framework to improve tracking performance and overcome the problem of scale ambiguity. While traditional geometric and hybrid approaches still achieve superior tracking performance, there are several fully learned SLAM frameworks [45, 46, 47, 23], which are superior in terms of reconstruction completeness. Jatavallabhula et al. [48] propose a differential optimizer which has the potential to bridge the gap between traditional and learning-based SLAM. A novel idea for deep-learning-based SLAM is proposed by Bloesch et al. [6]. The authors propose to learn a frame-wise code representation for the scene depth, which is the jointly optimized together with the camera pose. The work of Czarnowski et al. [7] is an extension of [6], where the code representation is integrated into a full SLAM system. Zuo et al. [8] make use of a similar code representation in a visual-inertial setup and furthermore feed sparse, tracked features into a DNN.

3 TANDEM

The proposed TANDEM is comprised of three components: monocular visual odometry (section 3.1), dense depth estimation with CVA-MVSNet (section 3.2), and volumetric mapping (suppl.). Figure 2a shows an overview of the system. The visual odometry utilizes the monocular video stream and the dense depth rendered from the 3D TSDF model to estimate camera poses in a sliding-window manner. Given the keyframes and their estimated poses, the proposed CVA-MVSNet predicts a dense depth map for the reference keyframe. To reconstruct a complete and globally consistent 3D model of the environment, the depth maps are then fused into the TSDF voxel grid [49] with voxel-hashing [28]. By seamlessly integrating these components, the resultant system TANDEM enables real-time tracking and high-quality dense mapping from a monocular camera. Further details, including on the TSDF volume initialization, are given in the supplementary material.

3.1 Visual Odometry

Estimating camera poses by tracking a sparse set of points across multiple frames has shown great performance in recent VO systems [39, 41]. Using more points for the joint optimization, how-

ever, does not necessarily further improve the accuracy of the estimated poses while significantly increases the runtime [39]. Therefore, in the proposed VO system we make use of a direct sparse windowed optimization back-end as described in Direct Sparse Odometry (DSO) [39]. However, we utilize dense depth maps rendered from the global TSDF model, which we build up incrementally, in the direct image alignment front-end. In numerous experiments, we confirm that this combination of dense tracking front-end and sparse back-end optimization significantly improves the tracking performance (cf. Table 1) while maintaining a fast runtime.

Dense Front-end Tracking. The front-end tracking provides camera-rate pose estimations and serves as initialization for the windowed optimization back-end. In the original DSO, a new frame is tracked against the last keyframe n by direct image alignment using a sparse depth map $\mathbf{D}_n^{\text{DSO}}[\mathbf{p}]$ generated from all points in the optimization window. This approach, however, lacks robustness (cf. Table 1) due to the sparsity of the depth map. We alleviate the issue by incorporating a dense depth map $\mathbf{D}_n^{\text{TSDF}}$ which is rendered from the constructed TSDF model. For each pixel $\mathbf{p}$ in the current keyframe n, we assign a depth value either based on the sparse VO points $\mathbf{D}_n^{\text{DSO}}[\mathbf{p}]$, if available, or based on the rendered dense depth $\mathbf{D}_n^{\text{TSDF}}[\mathbf{p}]$, otherwise. Due to the incrementally-built TSDF model, the combined depth buffer might not contain valid depth values for all pixels but it is much denser in comparison to using the sparse depth values only. The nearly-dense combined depth map is used for two-frame direct image alignment.

3.2 CVA-MVSNet

Let $\{(I_i, \mathbf{T}_i)\}_{i=1}^n$ be the set of active keyframes where I_i is the image of size (H, W) and $\mathbf{T}_i$ is the corresponding global pose estimated by the VO. CVA-MVSNet is based on the principles of multi-view stereo [50] and further leverages deep neural networks [22] to estimate a depth map for the reference frame I_{n-1}. CVA-MVSNet overcomes the prohibitive memory requirement of deep MVS networks by hierarchically estimating the depth using cascaded cost volumes and aggregates the deep features of all the keyframes effectively with a self-adaptive view aggregation module.

As shown in Figure 2b, the multi-scale deep features $\mathbf{F}_i^s$ of the keyframes are firstly extracted by 2D U-Nets with shared weights, where $i \in [1, n]$ is the frame index and $s \in [1, 3]$ is the scale index. As a result, $\mathbf{F}_i^s$ is of the shape (F^s, H^s, W^s) where F^s is the feature dimension of the scale s, $H^s = H/2^{3-s}$, and $W^s = W/2^{3-s}$. The depth map of the reference frame is estimated hierarchically with 3 stages each of which takes the set of features $\{\mathbf{F}_i^s\}_{i=1}^n$ as the inputs and predicts the reference depth map $\mathbf{D}^s$ of shape (H^s, W^s). For clarity, we first explain how a single stage estimates the depth and then describe how multiple stages are assembled hierarchically.

Single Stage Depth Estimation. For each stage, a cost volume $\mathbf{C}^s$ needs to be constructed using the deep features $\{\mathbf{F}_i^s\}_{i=1}^n$. For each pixel of the reference frame, we define D^s depth hypotheses, which results in a tensor $\mathbf{D}_{hyp}^s$ of shape (D^s, H^s, W^s). The deep features $\mathbf{F}_i^s$ of each frame are geometrically transformed with differentiable warping [51] using the depth hypotheses, the relative pose $\mathbf{T}_j^i = \mathbf{T}_i^{-1}\mathbf{T}_j$ and the camera intrinsics. As a result, a feature volume $\mathbf{V}_i^s$ of shape (F^s, D^s, H^s, W^s) is constructed for every frame.

In order to aggregate the information from multi-view feature volumes into one cost volume $\mathbf{C}^s$, most prior deep MVS methods treat different views equally and use a variance-based cost metric:

$$\mathbf{C}^s = \frac{\sum_{i=1}^n (\mathbf{V}_i^s - \bar{\mathbf{V}}^s)^2}{n}, \quad \text{where} \quad \bar{\mathbf{V}} = \frac{\sum_{i=1}^n \mathbf{V}_i^s}{n}. \tag{1}$$

However, in the sliding-window SLAM setting, the keyframes are not evenly distributed within the optimization window – typically the distance between newer keyframes is much smaller than between older keyframes. This causes considerable occlusion and non-overlapping images. The variance-based cost volume, which weighs different views equally, is thus inappropriate. To alleviate this issue, we employ self-adaptive view aggregation [27] to construct the cost volume:

$$\mathbf{C}^s = \frac{\sum_{i=1, i\neq j}^n (1 + \mathbf{W}_i^s) \odot (\mathbf{V}_i^s - \mathbf{V}_j^s)^2}{n-1}, \tag{2}$$

where the view aggregation weights $\mathbf{W}_i^s$ have the shape $(1, D^s, H^s, W^s)$ and $\odot$ is element-wise multiplication with broadcasting. The view aggregation weights $\mathbf{W}_i^s$ are estimated by a shallow 3D convolutional network for each $\mathbf{V}_i^s$ separately by taking $(\mathbf{V}_i^s - \mathbf{V}_j^s)^2$ as the input. This aggregation module allows the network to adaptively downweight erroneous information.

The cost volume $\mathbf{C}^s$ is then regularized using a 3D U-Net and finally passed through a softmax non-linearity to obtain a probability volume $\mathbf{P}^s$ of shape (D^s, H^s, W^s). Given the per-pixel depth hypotheses $\mathbf{D}^s_{hyp}$ of shape (D^s, H^s, W^s) the estimated depth is given as the expected value

$$\mathbf{D}^s[h, w] = \sum_{d=1}^{D} \mathbf{P}^s[d, h, w] \cdot \mathbf{D}^s_{hyp}[d, h, w]. \tag{3}$$

Hierarchical Depth Estimation. The network leverages the depth estimated from the previous stage $\mathbf{D}^{s-1}(s > 1)$ to define a fine-grained depth hypothesis tensor $\mathbf{D}^s_{hyp}$ with a small D^s. Since no prior stage exists for the first stage, each pixel of $\mathbf{D}^1_{hyp}$ has the same depth range defined by $[d_{min}, d_{max}]$ with $D^1 = 48$ depth values. For the later stages ($s > 1$), the depth $\mathbf{D}^{s-1}$ is upsampled and then used as a prior to define $\mathbf{D}^s_{hyp}$. Specifically, for the pixel location (h, w), $\mathbf{D}^s_{hyp}(\cdot, h, w)$ is defined using the upsampled $\mathbf{D}^{s-1}(h, w)$ as the center and then sampled D^s values around it using a pre-defined offset [26]. In this way, fewer depth planes are needed for the stage with a higher resolution, i.e., $D^1 \geq D^2 \geq D^3$. We train the network using the $L1$ loss applied on all three stages with respect to the ground-truth depth and use the sum as the final loss function.

3.3 Implementation Details

To guarantee real-time execution, TANDEM leverages parallelism on multiple levels. Dense tracking and bundle adjustment are executed in parallel threads on the CPU while, asynchronously and in parallel, TSDF fusion and DNN inference are run on the GPU. We train our CVA-MVSNet in PyTorch [52] and perform inference in C++ using TorchScript.

TANDEM can processes images at ca. 20 FPS while running on a desktop with an Nvidia RTX 2080 super with 8 GB VRAM, and an Intel i7-9700K CPU. This includes tracking and dense TSDF mapping but no visualization or mesh generation. We refer to the supplementary for further details, including how to potentially scale the network for deployment on embedded platforms.

4 Experimental Results

As TANDEM is a complete dense SLAM system, we evaluate it for both monocular camera tracking and dense 3D reconstruction. Specifically, for the camera tracking, we compare with state-of-the-art traditional sparse monocular odometry, DSO [39] and ORB-SLAM [41], as well as learning-based dense SLAM methods, DeepFactors [7] and CodeVIO [8]. For the 3D reconstruction, we compare with a state-of-the-art deep multi-view stereo method, Cas-MVSNet [26], end-to-end reconstruction method, Atlas [9], learning-based dense SLAM methods, CNN-SLAM [5], DeepFactors [7], and CodeVIO [8], as well as iMAP [34], a recently proposed RGB-D dense SLAM method using a deep implicit map representation [53, 54].

In the following, we will first introduce the datasets we use for training and evaluation. Note that only CVA-MVSNet needs to be trained while the dense tracking part of TANDEM is purely optimization-based and does not require training on specific datasets. Then, the ablation study for TANDEM demonstrates different design choices. In the end, we show quantitative and qualitative comparisons with other state-of-the-art methods. Due to the limited space, we demonstrate only part of the conducted evaluation and refer to the supplementary material for additional experiments.

4.1 Datasets

Training sets. We train two models for CVA-MVSNet: One on the real-world **ScanNet** [55] dataset and the other one on the synthetic **Replica** dataset [11]. The ScanNet dataset consists of 1513 indoor scenes and we use the official train and test split for training CVA-MVSNet to give a fair comparisons with DeepFactors and Atlas. However, the geometry and texture in ScanNet show noticeable artifacts and incompleteness [11], which limits its potential to training high-quality dense reconstruction methods. To complement the ScanNet dataset, we build upon the recently proposed Replica dataset [11], which consists of 18 photorealistic scenes. These scenes were captured from real-world rooms using a state-of-the-art 3D reconstruction pipeline and show very high-quality texture and geometry. Because the authors did not release any sequences, we extend the dataset by manually creating realistic camera trajectories that yield 55 thousand poses and images.

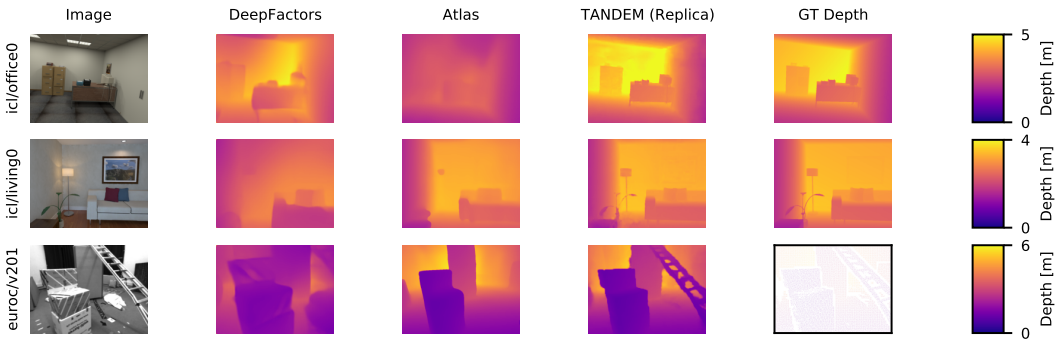

Figure 3: Depth comparison for DeepFactors [7], Atlas [9], and TANDEM on unseen sequences. TANDEM produces finer-scale details, e.g. the plant in the second row, or the ladder in the third row. For EuRoC only sparse ground-truth depth is available. A high-resolution version of this figure can be found in the supplementary material.

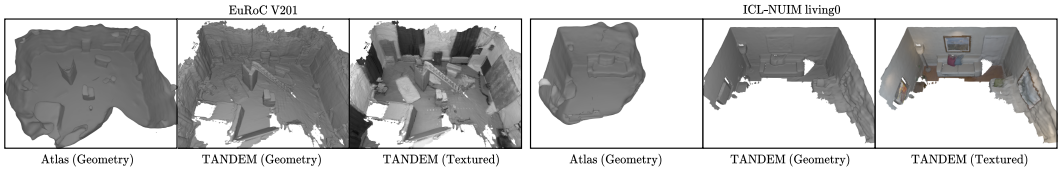

Figure 4: Qualitative comparison of Atlas [9] and TANDEM on unseen sequences. Atlas does not construct textured meshes, so we also render the pure geometry from TANDEM for comparison.

Evaluation sets. We use the **ICL-NUIM** [13] dataset and the Vicon Room sequences of the **EuRoC** dataset [12] for evaluating the tracking and the dense 3D reconstruction. Note that TANDEM is not trained on either of the datasets. ICL-NUIM is a synthetic indoor dataset with pose and dense depth ground-truth. It contains low-texture scenes which are challenging for monocular visual odometry and dense depth estimation. EuRoC is a real-world dataset recorded by a micro aerial vehicle (MAV).

4.2 Camera Pose Estimation

We evaluate TANDEM for pose estimation against other state-of-the-art monocular SLAM methods on EuRoC and ICL-NUIM. On EuRoC, we evaluate against DSO [39], ORB-SLAM2 [41], DeepFactors [7], and CodeVIO [8] uses a camera and an IMU sensor. Note that we turn off the global optimization and relocalization of ORB-SLAM2 for a fair comparison. We also implement a variant of DSO (DSO + Dense Depth) which uses all the pixels of the dense depth maps estimated by CVA-MVSNet for the front-end direct image alignment. Note that the difference between TANDEM and DSO + Dense Depth is that TANDEM tracks against the *global 3D model* by rendering the depth maps from the TSDF grid. TANDEM achieves overall better tracking accuracy and robustness than the other monocular methods on both ICL-NUIM and EurRoC. Due to the limited space, we show the results on EuRoC in Table 1 of the main paper and kindly refer to the supplementary material for the results on ICL-NUIM where we also show the comparision with DeepTAM [23].

All the methods except for CodeVIO [8] are run five times for each sequence and reported with the mean RMSE error and standard deviation in terms of absolute pose estimations after Sim(3) alignment with ground-truth. For CodeVIO, we directly take the numbers reported in their paper. The comparison with DSO and DSO + Dense Depth indicates that the proposed dense tracking against the global 3D model improves the camera pose estimations, especially on the more challenging sequences (V102 and V202). However, we should admit that TANDEM still cannot compete with CodeVIO which uses an IMU sensor for pose estimations.

4.3 Ablation Study

We conduct the ablation study of CVA-MVSNet on the test split of Replica and show the results in Table 2. Specifically, we evaluate the effectiveness of using the full VO window with 7

Table 1: Pose evaluation on EuRoC [12]. All the methods are Sim(3) aligned w.r.t. the ground-truth trajectories. The mean absolute pose errors and the standard deviations over five runs are shown.

Sequence	CodeVIO[8]	DeepFactors[7]	DSO [39]	ORB-SLAM2 [41]	DSO+Dense Depth	Ours
EuRoC/V101	**0.06** (-)	1.48 (±0.134)	0.10 (±0.006)	0.31 (±0.22)	0.09 (±0.002)	0.09 (±0.001)
EuRoC/V102	**0.07** (-)	Lost	0.27 (±0.017)	0.11 (±0.05)	0.28 (±0.015)	0.17 (±0.006)
EuRoC/V201	**0.10** (-)	1.06 (±0.441)	0.09 (±0.005)	1.40 (±0.211)	0.09 (±0.003)	0.09 (±0.002)
EuRoC/V202	**0.06** (-)	1.89 (±0.019)	0.21 (±0.020)	0.84 (±0.648)	0.19 (±0.022)	0.12 (±0.009)

Table 2: Ablation study of CVA-MVSNet on Replica [11]. Using all keyframes within the VO window (*Win*) does not improve the baseline. However, combining *Win* with view aggregation (*VA*) yields more accurate results at the cost of increased inference runtime and memory. By reducing the number of depth planes (*S*) from $(48, 32, 8)$ to $(48, 4, 4)$ we retain high quality and guarantee the real-time performance of TANDEM. Best shown in **bold** and second best shown underlined.

	Win	VA	S	Abs↓ [cm]	a_1 ↑ [%]	a_2 ↑ [%]	a_3 ↑ [%]	Time↓ [ms]	Mem.↓ [MiB]
baseline [26]				2.64	98.64	82.33	20.12	**142**	3447
+ VO window	✓			2.64	98.39	83.55	20.56	215	4117
+ View aggregation	✓	✓		**1.92**	**99.00**	**88.59**	26.03	288	4117
+ Fewer depth planes	✓	✓	✓	2.33	98.51	86.93	**26.09**	158	**2917**

keyframes (Win), the view aggregation module (VA), and fewer depth planes (S) with $(48, 4, 4)$ for (D^1, D^2, D^3). The baseline method is the original Cas-MVSNet using 3 multi-view images as the inputs, no view aggregation module, and more depth planes $(48, 32, 8)$. We use the absolute difference (Abs), and the percentage of inliers with different thresholds (a_1, a_2, a_3) as the metrics for the depth map evaluation. Please refer to the supplementary material for the formulas of the metrics. In addition, we also show the inference time and the memory usage of different models. From the table, we can see that using the entire keyframe window with more frames does not improve the accuracy over the baseline model while increasing the runtime and memory usage. With the view aggregation module, the accuracy is significantly improved, but the runtime further increases. Using fewer depth planes does not show a significant drop in accuracy but improves the runtime and memory usage a lot. Therefore, to guarantee the real-time performance of TANDEM, we use the fewer-plane model as the final CVA-MVSNet and all other experiments in the paper are conducted with this model.

4.4 3D Reconstruction

We evaluate the reconstruction accuracy on both ICL-NUIM and EuRoC. On ICL-NUIM we compare with DeepFactors [7], CNN-SLAM [5], Atlas [9], and Cas-MVSNet [26]. Table 3 shows the evaluation results. Since Atlas, a pure 3D reconstruction method, does not estimate poses, we provide ground-truth poses as the input. Note that Atlas estimates a TSDF volume directly from a 3D CNN, so we render the depth maps for evaluation against other methods. CNN-SLAM, DeepFactors, and Atlas are trained on ScanNet. For Cas-MVSNet, we re-train it on the Replica dataset and use the same poses as for our CVA-MVSNet. We show the results of the evaluations for our ScanNet-trained model and our Replica-trained model to facilitate a fair comparison. The depth maps of monocular methods are aligned in scale based on the trajectory and further details are given in the supplementary. We use the a_1 metric as the major measurement for accuracy. From Table 3, we can see that our method shows a notable improvement in comparison to the other methods and delivers the best result on average. Note that CVA-MVSNet achieves better results with the model trained on the synthetic Replica than the model trained on ScanNet.

On EuRoC, we cannot compare with CNN-SLAM since the numbers on EuRoC are not provided on the paper and code is not publicly available. We further add CodeVIO [8] into the evaluation on EuRoC as it is a recent dense SLAM system and it was also evaluated on EuRoC. Please note that CodeVIO uses a monocular camera and an inertial sensor for tracking, while TANDEM and other SLAM methods rely only on monocular cameras. Table 4 shows the evaluation results.

We further evaluate TANDEM against iMAP [34], an RGB-D dense SLAM system that leverages deep implicit map representation. Please note two major differences between iMAP and TANDEM: on one hand, iMAP uses an RGB-D sensor while TANDEM needs only a monocular camera; on

Table 3: Depth evaluation on ICL-NUIM [13]. We show the percentage of pixels for which the estimated depth falls within 10% of the groundtruth value.

Sequence	CNN-SLAM [5]	DeepFactors [7]	Atlas [9]	Cas-MVSNet [26]	Ours (ScanNet)	Ours (Replica)
icl/office0	19.41	30.17	28.79	77.73	52.34	**84.04**
icl/office1	29.15	20.16	62.89	88.87	61.83	**91.18**
icl/living0	12.84	20.44	83.16	**97.06**	86.42	97.00
icl/living1	13.04	20.86	36.93	84.11	71.35	**90.62**
Average	19.77	30.17	66.93	86.94	67.99	**90.71**

Table 4: Depth evaluation on EuRoC [12]. We show the percentage of correct pixels d_1 as in [56].

Sequence	CodeVIO[8]	DeepFactors[7]	Atlas[9]	Cas-MVSNet[26]	Ours (ScanNet)	Ours (Replica)
EuRoC/V101	86.99	71.82	57.16	93.05	93.69	**94.25**
EuRoC/V102	78.65	X	**92.29**	88.03	89.62	90.50
EuRoC/V201	77.32	71.85	93.28	95.43	96.84	**97.17**
EuRoC/V202	71.98	68.26	64.33	93.16	92.65	**95.68**
Average	78.74		76.77	92.42	93.20	**94.40**

Table 5: Comparison to iMAP [34]. TANDEM shows comparable performance to iMAP, which uses RGB-D data, but no training prior to scanning. The mesh-based 3D metrics are as in [34].

	room-1			office-4		
	Acc [cm]	Comp [cm]	CR [%]	Acc [cm]	Comp [cm]	CR [%]
iMAP	**3.69**	4.87	**83.45**	4.83	6.59	**77.63**
TANDEM	4.26	**4.71**	81.95	**3.76**	**6.11**	74.66

the other hand, the DNN of iMAP does not require any pre-training and it is trained purely online with the RGB-D inputs, while the depth estimation network of TANDEM requires offline training. Since iMAP was also evaluated on Replica, we, therefore, compare TANDEM with iMAP on the two sequences of their dataset which are not included in the training set of our Replica split. We use the evaluation metrics from iMAP and show the results in Table 5. In general, TANDEM achieves similar results to iMAP while using a monocular camera.

In Figure 3 we show qualitative depth maps estimated by DeepFactors, Atlas, and TANDEM. Both DeepFactors and Atlas can recover the geometry of the underlying scene well, but our method generally manages to capture more fine-scale details. We further show the complete scene reconstruction as meshes in Figure 4. As DeepFactors does not generate a complete 3D model by itself, we only compare TANDEM with Atlas for this experiment. From the figure we can see that, similarly to the depth maps, TANDEM is able to reconstruct more fine-scale details than Atlas.

5 Conclusion

We presented TANDEM, a real-time dense monocular SLAM system with a novel design that couples direct photometric visual odometry and deep multi-view stereo. In particular, we propose CVA-MVSNet which leverages the whole keyframe window effectively and predicts high-quality depth maps. Further, the proposed dense tracking scheme bridges camera pose estimation and dense 3D reconstruction by tracking against the global 3D model created with TSDF fusion. The quantitative and qualitative experiments show that TANDEM achieves better results than other state-of-the-art methods for both 3D reconstruction and visual odometry on synthetic and real-world data. We believe that TANDEM further bridges the gap between RGB-D mapping and monocular mapping.

Acknowledgments

We thank the anonymous reviewers for providing helpful comments that improved the paper. We express our appreciation to our colleagues, who have supported us, specifically we thank Mariia

Gladkova (Technical University of Munich) and Simon Klenk (Technical University of Munich) for proof reading, as well as, Stefan Leutenegger (Technical University of Munich & Imperial College London) and Sotiris Papatheodorou (Imperial College London) for their help with setting up a demo for the conference. We thank the authors of iMAP, specifically Edgar Sucar (Imperial College London), for providing us with evaluation data and scripts from their paper.

References

[1] R. A. Newcombe, A. Fitzgibbon, S. Izadi, O. Hilliges, D. Molyneaux, D. Kim, A. J. Davison, P. Kohi, J. Shotton, and S. Hodges. KinectFusion: Real-time dense surface mapping and tracking. In *IEEE International Symposium on Mixed and Augmented Reality*, 2011.

[2] C. Kerl, J. Sturm, and D. Cremers. Dense visual SLAM for RGB-D cameras. In *IEEE International Conference on Intelligent Robots and Systems (IROS)*, 2013.

[3] T. Whelan, S. Leutenegger, R. S. Moreno, B. Glocker, and A. Davison. ElasticFusion: Dense SLAM without a pose graph. In *Robotics: Science and Systems (RSS)*, 2015.

[4] J. Zhang and S. Singh. Visual-lidar odometry and mapping: low-drift, robust, and fast. In *IEEE International Conference on Robotics and Automation (ICRA)*, 2015.

[5] K. Tateno, F. Tombari, I. Laina, and N. Navab. CNN-SLAM: Real-time dense monocular SLAM with learned depth prediction. In *IEEE Conference on Computer Vision and Pattern Recognition (CVPR)*, 2017.

[6] M. Bloesch, J. Czarnowski, R. Clark, S. Leutenegger, and A. J. Davison. CodeSLAM - learning a compact, optimisable representation for dense visual SLAM. In *IEEE Conference on Computer Vision and Pattern Recognition (CVPR)*, 2018.

[7] J. Czarnowski, T. Laidlow, R. Clark, and A. J. Davison. DeepFactors: Real-time probabilistic dense monocular SLAM. *IEEE Robotics and Automation Letters*, 2020.

[8] X. Zuo, N. Merrill, W. Li, Y. Liu, M. Pollefeys, and G. Huang. CodeVIO: Visual-inertial odometry with learned optimizable dense depth. *arXiv preprint arXiv:2012.10133*, 2020.

[9] Z. Murez, T. van As, J. Bartolozzi, A. Sinha, V. Badrinarayanan, and A. Rabinovich. Atlas: End-to-end 3D scene reconstruction from posed images. In *European Conference on Computer Vision (ECCV)*, 2020.

[10] C. Tang and P. Tan. BA-Net: Dense bundle adjustment networks. In *International Conference on Learning Representations (ICLR)*, 2019.

[11] J. Straub, T. Whelan, L. Ma, Y. Chen, E. Wijmans, S. Green, J. J. Engel, R. Mur-Artal, C. Ren, S. Verma, A. Clarkson, M. Yan, B. Budge, Y. Yan, X. Pan, J. Yon, Y. Zou, K. Leon, N. Carter, J. Briales, T. Gillingham, E. Mueggler, L. Pesqueira, M. Savva, D. Batra, H. M. Strasdat, R. D. Nardi, M. Goesele, S. Lovegrove, and R. Newcombe. The Replica dataset: A digital replica of indoor spaces. *arXiv preprint arXiv:1906.05797*, 2019.

[12] M. Burri, J. Nikolic, P. Gohl, T. Schneider, J. Rehder, S. Omari, M. W. Achtelik, and R. Siegwart. The euroc micro aerial vehicle datasets. *The International Journal of Robotics Research*, 35(10):1157–1163, 2016.

[13] A. Handa, T. Whelan, J. McDonald, and A. J. Davison. A benchmark for RGB-D visual odometry, 3D reconstruction and SLAM. In *IEEE International Conference on Robotics and Automation (ICRA)*, 2014.

[14] Y. Furukawa and J. Ponce. Accurate, dense, and robust multiview stereopsis. *IEEE Transactions on Pattern Analysis and Machine Intelligence*, 2010.

[15] J. Stühmer, S. Gumhold, and D. Cremers. Real-time dense geometry from a handheld camera. In *Pattern Recognition - 32nd DAGM Symposium*, 2010.

[16] J. L. Schönberger, E. Zheng, J.-M. Frahm, and M. Pollefeys. Pixelwise view selection for unstructured multi-view stereo. In *European Conference on Computer Vision (ECCV)*, 2016.

[17] S. Weder, J. L. Schönberger, M. Pollefeys, and M. R. Oswald. RoutedFusion: Learning real-time depth map fusion. In *IEEE/CVF Conference on Computer Vision and Pattern Recognition (CVPR)*, June 2020.

[18] M. Ji, J. Gall, H. Zheng, Y. Liu, and L. Fang. SurfaceNet: An end-to-end 3D neural network for multiview stereopsis. In *IEEE International Conference on Computer Vision (ICCV)*, 2017.

[19] A. Kar, C. Häne, and J. Malik. Learning a multi-view stereo machine. In *Conference on Neural Information Processing Systems (NeurIPS)*, 2017.

[20] R. Chen, S. Han, J. Xu, and H. Su. Point-based multi-view stereo network. In *IEEE International Conference on Computer Vision (ICCV)*, 2019.

[21] P.-H. Huang, K. Matzen, J. Kopf, N. Ahuja, and J.-B. Huang. DeepMVS: Learning multi-view stereopsis. In *IEEE Conference on Computer Vision and Pattern Recognition (CVPR)*, 2018.

[22] Y. Yao, Z. Luo, S. Li, T. Fang, and L. Quan. MVSNet: Depth inference for unstructured multi-view stereo. In *European Conference on Computer Vision (ECCV)*, 2018.

[23] H. Zhou, B. Ummenhofer, and T. Brox. DeepTAM: Deep tracking and mapping. In *European Conference on Computer Vision (ECCV)*, 2018.

[24] Y. Hou, J. Kannala, and A. Solin. Multi-view stereo by temporal nonparametric fusion. In *Proceedings of the IEEE/CVF International Conference on Computer Vision*, pages 2651–2660, 2019.

[25] Y. Yao, Z. Luo, S. Li, T. Shen, T. Fang, and L. Quan. Recurrent MVSNet for high-resolution multi-view stereo depth inference. In *IEEE Conference on Computer Vision and Pattern Recognition (CVPR)*, 2019.

[26] X. Gu, Z. Fan, S. Zhu, Z. Dai, F. Tan, and P. Tan. Cascade cost volume for high-resolution multi-view stereo and stereo matching. In *IEEE Conference on Computer Vision and Pattern Recognition (CVPR)*, 2020.

[27] H. Yi, Z. Wei, M. Ding, R. Zhang, Y. Chen, G. Wang, and Y. Tai. Pyramid multi-view stereo net with self-adaptive view aggregation. In *European Conference on Computer Vision (ECCV)*, 2020.

[28] M. Niessner, M. Zollhöfer, S. Izadi, and M. Stamminger. Real-time 3D reconstruction at scale using voxel hashing. *ACM Transactions on Graphics (TOG)*, 2013.

[29] F. Steinbrücker, J. Sturm, and D. Cremers. Volumetric 3D mapping in real-time on a CPU. In *ICRA*, pages 2021–2028. IEEE, 2014.

[30] E. Bylow, J. Sturm, C. Kerl, F. Kahl, and D. Cremers. Real-time camera tracking and 3D reconstruction using signed distance functions. In *Robotics: Science and Systems (RSS)*, 2013.

[31] C. Kerl, J. Sturm, and D. Cremers. Robust odometry estimation for RGB-D cameras. In *IEEE International Conference on Robotics and Automation (ICRA)*, 2013.

[32] O. Kähler, V. A. Prisacariu, and D. W. Murray. Real-time large-scale dense 3D reconstruction with loop closure. In *European Conference on Computer Vision (ECCV)*, 2016.

[33] T. Schöps, T. Sattler, and M. Pollefeys. BAD SLAM: Bundle adjusted direct RGB-D SLAM. In *IEEE Conference on Computer Vision and Pattern Recognition (CVPR)*, 2019.

[34] E. Sucar, S. Liu, J. Ortiz, and A. Davison. iMAP: Implicit mapping and positioning in real-time. In *IEEE International Conference on Computer Vision (ICCV)*, 2021.

[35] R. A. Newcombe, S. J. Lovegrove, and A. J. Davison. DTAM: Dense tracking and mapping in real-time. In *IEEE International Conference on Computer Vision (ICCV)*, 2011.

[36] M. Pizzoli, C. Forster, and D. Scaramuzza. REMODE: Probabilistic, monocular dense reconstruction in real time. In *IEEE International Conference on Robotics and Automation (ICRA)*, 2014.

[37] G. Vogiatzis and C. Hernández. Video-based, real-time multi-view stereo. *Image and Vision Computing*, 29(7):434–441, 2011.

[38] J. Engel, T. Schöps, and D. Cremers. LSD-SLAM: large-scale direct monocular SLAM. In *European Conference on Computer Vision (ECCV)*, 2014.

[39] J. Engel, V. Koltun, and D. Cremers. Direct sparse odometry. *IEEE Transactions on Pattern Analysis and Machine Intelligence*, 2018.

[40] R. Mur-Artal and J. D. Tardos. Probabilistic semi-dense mapping from highly accurate feature-based monocular SLAM. In *Robotics: Science and Systems (RSS)*, 2015.

[41] R. Mur-Artal, J. M. M. Montiel, and J. D. Tardos. ORB-SLAM: A versatile and accurate monocular SLAM system. *IEEE Transactions on Robotics*, 2015.

[42] T. Schöps, T. Sattler, C. Häne, and M. Pollefeys. Large-scale outdoor 3D reconstruction on a mobile device. *Computer Vision and Image Understanding*, 2017.

[43] N. Yang, R. Wang, J. Stuckler, and D. Cremers. Deep virtual stereo odometry: Leveraging deep depth prediction for monocular direct sparse odometry. In *European Conference on Computer Vision (ECCV)*, 2018.

[44] N. Yang, L. von Stumberg, R. Wang, and D. Cremers. D3VO: Deep depth, deep pose and deep uncertainty for monocular visual odometry. In *IEEE Conference on Computer Vision and Pattern Recognition (CVPR)*, 2020.

[45] T. Zhou, M. Brown, N. Snavely, and D. G. Lowe. Unsupervised learning of depth and ego-motion from video. In *IEEE Conference on Computer Vision and Pattern Recognition (CVPR)*, 2017.

[46] Z. Yin and J. Shi. GeoNet: Unsupervised learning of dense depth, optical flow and camera pose. In *IEEE Conference on Computer Vision and Pattern Recognition (CVPR)*, 2018.

[47] H. Zhan, R. Garg, C. S. Weerasekera, K. Li, H. Agarwal, and I. M. Reid. Unsupervised learning of monocular depth estimation and visual odometry with deep feature reconstruction. In *IEEE Conference on Computer Vision and Pattern Recognition (CVPR)*, 2018.

[48] K. M. Jatavallabhula, G. Iyer, and L. Paull. ∇SLAM: Dense SLAM meets automatic differentiation. In *IEEE International Conference on Robotics and Automation (ICRA)*, pages 2130–2137, 2020.

[49] B. Curless and M. Levoy. A volumetric method for building complex models from range images. In *Conference on Computer Graphics and Interactive Techniques (SIGGRAPH)*, 1996.

[50] Y. Furukawa and C. Hernández. Multi-view stereo: A tutorial. *Foundations and Trends® in Computer Graphics and Vision*, 9(1-2):1–148, 2015.

[51] M. Jaderberg, K. Simonyan, A. Zisserman, and K. Kavukcuoglu. Spatial transformer networks. In *Conference on Neural Information Processing Systems (NeurIPS)*, 2015.

[52] A. Paszke, S. Gross, F. Massa, A. Lerer, J. Bradbury, G. Chanan, T. Killeen, Z. Lin, N. Gimelshein, L. Antiga, A. Desmaison, A. Kopf, E. Yang, Z. DeVito, M. Raison, A. Tejani, S. Chilamkurthy, B. Steiner, L. Fang, J. Bai, and S. Chintala. Pytorch: An imperative style, high-performance deep learning library. In *Conference on Neural Information Processing Systems (NeurIPS)*, 2019.

[53] J. J. Park, P. Florence, J. Straub, R. Newcombe, and S. Lovegrove. DeepSDF: Learning continuous signed distance functions for shape representation. In *Proceedings of the IEEE/CVF Conference on Computer Vision and Pattern Recognition*, pages 165–174, 2019.

[54] L. Mescheder, M. Oechsle, M. Niemeyer, S. Nowozin, and A. Geiger. Occupancy networks: Learning 3D reconstruction in function space. In *Proceedings of the IEEE/CVF Conference on Computer Vision and Pattern Recognition*, pages 4460–4470, 2019.

[55] A. Dai, A. X. Chang, M. Savva, M. Halber, T. Funkhouser, and M. Nießner. ScanNet: Richly-annotated 3D reconstructions of indoor scenes. In *IEEE Conference on Computer Vision and Pattern Recognition (CVPR)*, 2017.

[56] D. Eigen, C. Puhrsch, and R. Fergus. Depth map prediction from a single image using a multi-scale deep network. In Z. Ghahramani, M. Welling, C. Cortes, N. D. Lawrence, and K. Q. Weinberger, editors, *Conference on Neural Information Processing Systems (NeurIPS)*, pages 2366–2374. Curran Associates, 2014.

[57] R. Newcombe. *Dense visual SLAM*. PhD thesis, Imperial College London, UK, 2012.

[58] K. Kawaguchi, L. P. Kaelbling, and Y. Bengio. Generalization in deep learning. *CoRR*, abs/1710.05468, 2017.

[59] Y. Yao, Z. Luo, S. Li, J. Zhang, Y. Ren, L. Zhou, T. Fang, and L. Quan. Blendedmvs: A large-scale dataset for generalized multi-view stereo networks. In *IEEE Conference on Computer Vision and Pattern Recognition (CVPR)*, 2020.

[60] C. Cai, M. Poggi, S. Mattoccia, and P. Mordohai. Matching-space stereo networks for cross-domain generalization. In *3DV*, 2020.

[61] F. Zhang, X. Qi, R. Yang, V. Prisacariu, B. Wah, and P. Torr. Domain-invariant stereo matching networks. In *European Conference on Computer Vision (ECCV)*, 2020.

[62] H. Xu, Z. Zhou, Y. Qiao, W. Kang, and Q. Wu. Self-supervised multi-view stereo via effective co-segmentation and data-augmentation. In *AAAI Conference on Artificial Intelligence*, 2021.

[63] M. Poggi, A. Tonioni, F. Tosi, S. Mattoccia, and L. Di Stefano. Continual adaptation for deep stereo. *IEEE Transactions on Pattern Analysis and Machine Intelligence (PAMI)*, 2021.

[64] F. Wimbauer, N. Yang, L. von Stumberg, N. Zeller, and D. Cremers. Monorec: Semi-supervised dense reconstruction in dynamic environments from a single moving camera. In *IEEE Conference on Computer Vision and Pattern Recognition (CVPR)*, 2021.

[65] D. Schubert, N. Demmel, V. Usenko, J. Stückler, and D. Cremers. Direct sparse odometry with rolling shutter. In *European Conference on Computer Vision (ECCV)*, 2018.

[66] C. Kerl, J. Stückler, and D. Cremers. Dense continuous-time tracking and mapping with rolling shutter RGB-D cameras. In *IEEE International Conference on Computer Vision (ICCV)*, 2015.

[67] H. Strasdat, J. M. M. Montiel, and A. J. Davison. Visual SLAM: why filter? *Image Vis. Comput.*, 30(2):65–77, 2012.

[68] S. Ioffe and C. Szegedy. Batch normalization: Accelerating deep network training by reducing internal covariate shift. In *International Conference on Machine Learning (ICML)*, 2015.

[69] K. Fukushima and S. Miyake. Neocognitron: A self-organizing neural network model for a mechanism of visual pattern recognition. In *Competition and cooperation in neural nets*, 1982.

[70] V. Nair and G. E. Hinton. Rectified linear units improve restricted boltzmann machines. In *International Conference on Machine Learning (ICML)*, 2010.

[71] D. P. Kingma and J. Ba. Adam: A method for stochastic optimization. In *International Conference on Learning Representations (ICLR)*, 2015.

[72] NVIDIA. TensorRT. https://developer.nvidia.com/tensorrt, 2018.

[73] N. Dasan, C. Gottbrath, and J. Park. PyTorch-TensorRT: Accelerating inference in PyTorch with TensorRT. In *GPU Technology Conference (GTC)*, 2020. Available at https://developer.nvidia.com/gtc/2020/video/s21671.

[74] T. Schöps, J. Engel, and D. Cremers. Semi-dense visual odometry for AR on a smartphone. In *International Symposium on Mixed and Augmented Reality (ISMAR)*, 2014.

Supplementary Material

A Introduction

In this supplementary material, we briefly introduce the volumetric mapping of TANDEM (Appendix B), discuss the initialization in Appendix C, show further experimental results (Appendix D), give more details regarding our experiments (Appendix E) and, finally, provide implementation details for TANDEM in Appendix F including the possibility to deploy TANDEM on an embedded device (cf. section F.3). Upon publication, we will release our code for TANDEM as well as the rendered Replica sequences to facilitate the reproduction of our results.

We also urge the readers to watch the **supplementary video** which shows the real-time demos of TANDEM running on the unseen sequences.

B Volumetric Mapping

We use TSDF fusion [49] to fuse the per-keyframe estimated depth maps into a globally consistent and dense 3D model. Storing the TSDF values within a dense voxel grid has a cubic memory requirement in the spatial resolution of the grid and is thus unpractical. We employ voxel hashing [28] to alleviate this issue. The TSDF fusion is run on the GPU to ensure real-time performance.

For each voxel of the grid we store the estimated TSDF value $D_i(x) \in \mathbb{R}$, the estimated RGB values $C_i(x) \in \mathbb{R}^3$, and the weight $W_i(x) \in \mathbb{R}$, where x indexes the 3D location and i indexes the time. After our CVA-MVSNet has predicted a new depth map, we iterate over all voxels within the truncation distance and update their stored quantities. Let $d_{i+1}(x) \in \mathbb{R}$ be the projective TSDF value of the voxel at x based on the depth map from the CVA-MVSNet. Furthermore, let $c_{i+1}(x)$ be the associated RGB value from the input image, then

$$D_{i+1}(x) = \frac{W_i(x)D_i(x) + d_{i+1}}{W_i(x) + 1}\,, \tag{4}$$

$$C_{i+1}(x) = \frac{W_i(x)C_i(x) + c_{i+1}}{W_i(x) + 1}\,, \tag{5}$$

$$W_{i+1}(x) = \min(W_i(x) + 1,\, 64)\,. \tag{6}$$

The weight $W_i(x)$ is truncated at 64 (cf. Equation 6) to ensure that new measurements can influence the estimated quantities and avoid over-saturation. Depth maps are rendered from the TSDF volume using raycasting [49] and used for the proposed dense front-end tracking.

Because TANDEM is a monocular, geometry-based method the overall scale of the scene is not observable. Therefore, the voxel grid is scaled with the same scale as the visual odometry. The grid uses a voxel size of 0.01 which roughly corresponds to $2.5cm$ depending on the exact scale of a particular scene and run. We use a truncation distance for the TSDF of 0.1 which roughly corresponds to $25cm$. The global scale ambiguity that is common to all monocular, geometry-based methods renders the voxel size scene dependent. For our experiments the scene scale does not vary considerably and therefore we use a fixed voxel size. However, when considering scenes of different extent, the voxel size and truncation distance have to be set accordingly, which is also necessary when running classical TSDF fusion. The internal scale of TANDEM is generally such that the mean depth of the sparse points in the first frame is approximately identity.

The CVA-MVSNet requires a minimum and maximum depth value for inference, which is usually given in the dataset. However, during the live operation of TANDEM, we do not know the relative scale between the world and our reconstruction. To facilitate the live operation of TANDEM, we choose a simple strategy: the minimum depth is set 0.01, which is small enough to capture all objects, and the maximum depth is initially set to ten times the mean depth of the sparse points. For each following invocation of the CVA-MVSNet, we set the maximum depth to 1.5 times the previous maximum depth estimated by the network, which ensures that the whole scene is covered while providing good depth resolution. We found this simple scheme to work well in our experiments.

C Initialization

The proposed CVA-MVSNet operates on a keyframe window and thus the tracking is initialized the same way as in DSO [39] with non-linear optimization on poses and the sparse depth. The TSDF volume is initialized to represent empty space, i.e. with zero weights $W_0(x) = 0 \ \forall x$. Because we use voxel hashing [28] to represent the TSDF volume, empty space can be represented very efficiently by not allocating any voxel blocks. After the first dense depth map is predicted and integrated into the TSDF volume, TANDEM uses the rendered nearly dense depth maps for tracking as can be seen from Figure 9.

D Further Experimental Results

We show the trajectory evaluation on ICL-NUIM in Figure 5 and Table 6. Similar to the evaluation on the EuRoC dataset in the main paper, we see that the proposed TANDEM shows better results than DSO and DeepFactors [7]. Furthermore, TANDEM performs favourably in comparison to the tracking component of DeepTAM [23] that uses ground truth depth maps. We compare the trajectories for DeepFactors and TANDEM on the office1 sequence of the ICL-NUIM dataset in Figure 6. In Figure 7 we reproduce Figure 3 from the main paper in higher resolution to enable closer inspection of the generated depth maps. Furthermore, we show additional qualitative depth map comparisons in Figure 8. In section D.1 we discuss failure cases and challenges for TANDEM. The nearly dense depth maps used for tracking by TANDEM and the sparse depth maps from the photometric bundle adjustment are shown in Figure 9 and Figure 10.

D.1 Failure Cases and Challenges

Dense monocular SLAM is a challenging problem [57] and most systems fail in certain scenarios or perform worse given certain challenges. Any system that involves deep learning has to consider the generalization capability of neural network since, for SLAM, the training and testing datasets will practically always differ. Pure rotational motion is a known challenge for both visual SLAM and 3D reconstruction due to the unobservability of depth. Dynamic scenes, rolling shutter, and geometric errors are well known failure cases in SLAM if they are not modelled explicitly. While some of the aforementioned failure cases and challenges can be overcome by explicit modelling or through employing different techniques for tracking or mapping, this often leads to an increase in runtime and system complexity. In the following, we describe the weaknesses and the failure cases of the proposed system in order to facilitate further research in this direction:

Neural Network Generalization Generalization of deep neural networks is well known to pose challenges [58] and a general solution has yet to be proposed. For deep MVS multiple remedies have been proposed, including diverse training datasets [59], specific architecture choices [60, 61], and self-supervised adaption [62, 63]. While our CVA-MVSNet already shows good generalization capabilities as it was trained on either the ScanNet or the Replica dataset and generalizes to the ICL-NUIM and EuRoC datasets, the error metrics are better for the training datasets. Although initial experiments with specific architectures as well as self-supervised adaption didn't show convincing results for our training and testing datasets, we consider this a good direction for future research. For practical applications we consider the utilization of diverse training data together with re-training for new scenarios the most promising direction.

Pure Rotational Motion Pure rotational motion is critical because the depth of a point cannot be inferred, which leads to problems for tracking as well as depth estimation using MVS. While some purely rotational motion can be handled by TANDEM if the system has been initialized well, rotation-only motion during initialization will lead to failure in tracking. We experimentally validate this using the sequence office0 from the ICL-NUIM dataset. This sequence contains highly rotational motion and thus the results of TANDEM and DSO are worse in comparison to the office1 sequence or the living room sequences (cf. Table 6). We investigate the effect of rotational motion during initialization by starting the office0 sequence at frame 300, which is followed by a rotation along the ceiling of the office. Although the subsequence is shorter than the full sequence, the mean RMSE of the absolute pose error for TANDEM increases from $0.056\,m$ to $0.354\,m$, which shows that rotational motion during initialization remains an open challenge.

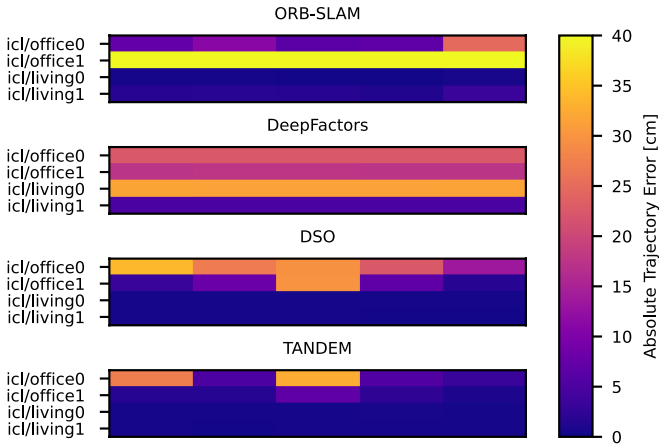

Figure 5: Trajectory evaluation on the ICL-NUIM dataset. Because all systems use monocular images we perform $\mathrm{Sim}(3)$ alignment w.r.t. the ground truth trajectories. We show the color-coded absolute trajectory error (ATE) for five runs. The results show that our dense tracking improves the robustness over DSO. DeepFactors produces nearly identical results for all five runs in this experiment but shows a higher median error.

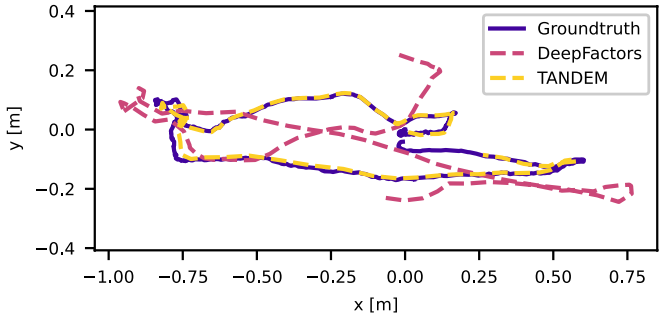

Figure 6: Estimated trajectories of DeepFactors and TANDEM on icl/office1. For both methods we select the run with the median error (cf. Figure 5).

Dynamic Scenes While the photometric bundle adjustment of TANDEM can implicitly handle dynamic objects if they constitute a relatively small fraction of the scene, the deep MVS fully relies on a static scene. Such scenarios are favourable for mono-to-depth-based methods as they are independent of the scene dynamics when predicting the depth. On the other hand, dynamic objects can be explicitly modelled within the cost volume [64].

Rolling Shutter The rolling shutter effect is known to be problematic for direct SLAM because not all pixels correspond to the same time and thus the same pose [65]. To investigate the effect of rolling shutter on TANDEM we use the ICL-NUIM living room sequences with synthetic rolling shutter proposed in [66]. For the sequences living0 and living1 the mean ATE RMSE increases from $0.006\,m$ to $0.018\,m$ and from $0.005\,m$ to $0.074\,m$, respectively.

Geometric Error Photometric methods are susceptible to geometric errors, e.g. from an inaccurate camera calibration, because these geometric errors are, in contrast to feature-based methods, not modeled explicitly. We simulate geometric errors by using an incorrect calibration for the ICL-NUIM living room sequences, specifically we add $5\,px$ to f_x, f_y, c_x, and c_y. For the sequences living0 and living1 the mean ATE RMSE increases from $0.006\,m$ to $0.041\,m$ and from $0.005\,m$ to $0.026\,m$, respectively.

Table 6: Pose evaluation on ICL-NUIM [13]. All the methods except DeepTAM are $\mathrm{Sim}(3)$ aligned w.r.t. the ground-truth trajectories. The mean absolute pose errors in meters and the standard deviations over five runs are shown. †For DeepTAM the official implementation contains only a pure tracking mode that requires ground truth depth maps for tracking, therefore, $\mathrm{SE}(3)$ alignment is performed because the scale is observable through the depth maps. Note that we show the result of a single run for DeepTAM since the results are consistent across multiple runs.

Sequence	DeepTAM† [23]	DeepFactors [7]	DSO [39]	TANDEM
icl/office0	<u>0.086</u> (-)	0.226 ($\pm$ 0.000)	0.270 ($\pm$ 0.070)	**0.056** ($\pm$ 0.126)
icl/office1	<u>0.030</u> (-)	0.175 ($\pm$ 0.001)	0.069 ($\pm$ 0.102)	**0.017** ($\pm$ 0.021)
icl/living0	0.025 (-)	0.315 ($\pm$ 0.001)	**0.006** ($\pm$ 0.000)	<u>0.006</u> ($\pm$ 0.000)
icl/living1	0.034 (-)	0.049 ($\pm$ 0.000)	<u>0.005</u> ($\pm$ 0.000)	**0.005** ($\pm$ 0.000)

E Experimental Details

E.1 Poses and Alignment

For the ablation study, we use ground-truth poses and a fixed set of keyframe windows to enable a fair and accurate comparison.

For the depth evaluation on ICL-NUIM and EuRoC, we run our visual odometry once to generate poses as well as keyframe windows. We use the same poses and keyframe windows to evaluate CasMVSNet, Ours (ScanNet), and Ours (Replica) to enable a fair and accurate comparison. Evaluating based on the full system would introduce significant non-determinism into the results. Because TANDEM is a monocular method, we use the scale estimated from the Sim(3) alignment of the trajectory to scale the depth maps. Since DeepFactors does not estimate very accurate poses on the EuRoC dataset (cf. Table 4 in the main paper), we scale align each depth map individually using the median scale between the ground-truth depth map and the predicted depth map. This procedure potentially overestimates the accuracy of DeepFactors, which is important to note when comparing with other methods.

For the comparison to iMAP, we use the Sim(3) alignment of the trajectory of TANDEM and the ground truth trajectory to transform the mesh into the same coordinate frame as the reference.

For the comparison on EuRoC we rectify the images s.t. the resulting images have resolution 640×480 and evaluate all methods except CodeVIO on the same rectified images for a fair comparison. For CodeVIO no public source code is available and we thus use the numbers published by the authors. Using a different rectification protocol can result in different results, which is often not obvious from the paper.

E.2 Depth Evaluation Metrics

For the following we will use y_i^* to denote the ground-truth depth value in meters and y_i to denote the corresponding predicted depth value. All metrics are computed per image first and then the average is taken over all images within the sequence. We let the index $i = 1, \dots, N$ enumerate all pixels with valid ground-truth depth for a given image. Note that thus there holds $y_i^* > 0$, $\forall i$.

The paper uses inconsistent metrics, e.g. a_1 and d_1, because prior works, e.g. DeepFactors and CodeVIO, used inconsistent metrics. Additionally, for some prior works, e.g. CodeVIO and CNN-SLAM, the source code is not available and therefore we cannot evaluate all methods using one consistent metric.

For the comparison on ICL-NUIM we follow DeepFactors and use the a_1 metric

$$a_1 = \frac{100}{N} \sum_{i=1}^{N} \mathbb{1}(|y_i - y_i^*|/y_i^* < 0.1)\,, \tag{7}$$

where $\mathbb{1}(\cdot)$ is the indicator function. The a_1 metric gives the percentage of pixels for which the estimated depth falls within 10% of the ground-truth depth.

For the ablation study, we follow DeepFactors and use the a_1 metric. We found that this metric is saturated because all configurations reach more than 98% and thus also show the stricter a_2 and a_3

metrics defined by

$$a_2 = \frac{100}{N} \sum_{i=1}^{N} \mathbb{1}(|y_i - y_i^*|/y_i^* < 0.01)\,, \tag{8}$$

$$a_3 = \frac{100}{N} \sum_{i=1}^{N} \mathbb{1}(|y_i - y_i^*|/y_i^* < 0.001)\,. \tag{9}$$

The a_2 and a_3 metrics give the percentage of pixels for which the estimated depth falls within 1% and 0.1% of the ground truth depth. Additionally, we show the mean absolute error in centimeters

$$Abs = \frac{100}{N} \sum_{i=1}^{N} |y_i - y_i^*|\,. \tag{10}$$

For the comparison on EuRoC we follow CodeVIO and use the d_1 metric as introduced by Eigen et al. [56]

$$d_1 = \frac{100}{N} \sum_{i=1}^{N} \mathbb{1}\Big(\max(\frac{y_i}{y_i^*}, \frac{y_i^*}{y_i}) < 1.25\Big)\,. \tag{11}$$

F Implementation Details

F.1 CVA-MVSNet

We list all the hyperparameters and their corresponding values in Table 10.

Architecture. The proposed CVA-MVSNet consists of three trainable components: the feature extraction network (cf. Table 7), the view aggregation network (cf. Table 8), and the cost regularization network (cf. Table 9). The feature extraction network takes as input each frame I_i and outputs the corresponding multi-scale feature maps $\mathbf{F}_i^s$, which are denoted by `out.stage1`, `out.stage2`, `out.stage3` in Table 7. The weights are shared for all frames. The view aggregation network takes as inputs the single frame cost volumes $(\mathbf{V}_i^s - \mathbf{V}_j^s)^2$ and outputs the aggregation weights $\mathbf{W}_i^s$. The weights are shared for all frames but are not shared for the three stages. The cost regularization network takes as input the aggregated cost volume

$$\mathbf{C}^s = \frac{\sum_{i=1, i\neq j}^{n} (1 + \mathbf{W}_i^s) \odot (\mathbf{V}_i^s - \mathbf{V}_j^s)^2}{n-1}\,,$$

and outputs the probability volume $\mathbf{P}^s$. There is a single network for all frames and the weights are not shared for the three stages.

F.2 Runtime

We report the mean runtimes for the single components of TANDEM in Table 11. Overall, TANDEM requires an average of 47 ms of processing time per frame, which gives a throughput of ca. 21 FPS. Additionally, Table 11 shows that using asynchronicity and parallelism between CPU and GPU is necessary to achieve real-time capability.

F.3 Deployment on an Embedded Device

For a SLAM system in the context of mobile robotics the deployment to an embedded platform is necessary for operation in the real world, if no uninterrupted connection to a server is available to offload computation. While we consider the actual deployment to an embedded system outside the scope of this research work, we show in the following that such a deployment is possible while maintaining accurate results.

An embedded system can benefit from software optimizations such as 16-bit float inference or NVIDIA TensorRT [72], which can bring speedups of up to $2\times$ and $2.5\times$, respectively [73]. However, we consider these engineering-focused optimizations outside the scope of this work.

Table 7: Feature extraction network. Layers are 2D convolutions or nearest neighbor interpolation with a scale factor 2, which we denote by $\uparrow$. For all layers we show the input and the channels (**chns**). For convolutions, we additionally show the kernel size (**k**), the stride (**s**), the padding (**p**), if the layer uses batch normalization (**bn**), and the activation function (**act**). Only the layers `skip.stage2` and `skip.stage3` have a bias term. We use batch normalization before the activation function.

Layer	input	k	s	p	chns	bn	act
`conv0.0`	`image`	3	1	1	$3 \rightarrow 8$	✓	ReLU
`conv0.1`	`conv0.0`	3	1	1	$8 \rightarrow 8$	✓	ReLU
`conv1.0`	`conv0.1`	5	2	2	$8 \rightarrow 16$	✓	ReLU
`conv1.1`	`conv1.0`	3	1	1	$16 \rightarrow 16$	✓	ReLU
`conv1.2`	`conv1.1`	3	1	1	$16 \rightarrow 16$	✓	ReLU
`conv2.0`	`conv1.2`	5	2	2	$16 \rightarrow 32$	✓	ReLU
`conv2.1`	`conv2.0`	3	1	1	$32 \rightarrow 32$	✓	ReLU
`conv2.2`	`conv2.1`	3	1	1	$32 \rightarrow 32$	✓	ReLU
`out.stage1`	`conv2.2`	1	1	0	$32 \rightarrow 32$		
`skip.stage2`	`conv1.2`	1	1	0	$16 \rightarrow 32$		
`inter.stage2`	$\uparrow$ `conv2.2` + `skip.stage2`				$32 \rightarrow 32$		
`out.stage2`	`inter.stage2`	3	1	1	$32 \rightarrow 16$		
`skip.stage3`	`conv0.1`	1	1	0	$8 \rightarrow 32$		
`inter.stage3`	$\uparrow$ `inter.stage2` + `skip.stage3`				$32 \rightarrow 32$		
`out.stage3`	`inter.stage3`	3	1	1	$32 \rightarrow 8$		

Table 8: View aggregation network. All layers are 3D convolutions. We show the input, the kernel size (**k**), the stride (**s**), the padding (**p**), the channels (**chns**), if the layer uses batch normalization (**bn**), and the activation function (**act**). All layers have a bias term. We use batch normalization before the activation function. The single frame cost volumes (`single frame cost volume`) have 32 channels for stage 1, 16 channels for stage 2, and 8 channels for stage 3.

Layer	input	k	s	p	chns	bn	act
`conv0`	`single frame cost volume`	1	1	0	$(32, 16, 8) \rightarrow 1$	✓	ReLU
`conv1`	`conv0`	1	1	0	$1 \rightarrow 1$	✓	ReLU

The inference time for our CVA-MVSNet given in the main paper is 158 ms and decreases to 133 ms by switching from PyTorch 1.5 to PyTorch 1.9. The 2D feature extraction network is run on all images from the keyframe window, while for all but one image the feature maps have been computed before. This fact can be used to save computational cost, however, to simplify the implementation, we did not use this optimization for the timings in Table 1. If the feature extraction network is run for only one image, the overall inference time decreases from 133 ms to 118 ms.

For the EuRoC experiment in the main paper we use images of size 640×480, which is relatively high in comparison to the image size used by DeepFactors of 256×192. Using this smaller image size decreases the inference time from 118 ms to 26.5 ms, a 77.5% relative improvement. The model trained on 640×480 images can be used for any resolution due to the fully-convolutional and geometry-based CVA-MVSNet and achieves an absolute error of 6.52 cm on the Replica validation set in comparison to 2.33 cm for the full resolution. However, when evaluating on EuRoC using the lower resolution results in an average accuracy (d_1) of 91.43% in comparison to 94.40%. The much smaller difference is due to the domain shift and additionally due to the relative laxness of the d_1 metric. Overall, the lower-resolution model is computationally much more efficient at a reasonable accuracy decrease.

Finally, TANDEM produces new keyframes often and marginalizes them early, which has been shown to aid tracking [39, 41]. A new keyframe is created roughly every 5 frames and the MVS

Table 9: Cost regularization network. All layers are either 3D convolutions (`conv`) or 3D transposed convolutions (`convT`). For all layers, we show the input, the kernel size (**k**), the stride (**s**), the padding (**p**), the channels (**chns**), if the layer uses batch normalization (**bn**), and the activation function (**act**). For transposed convolutions we show the output padding (**op**). We use batch normalization before the activation function. No layer has a bias term. The stride S (cf. `conv5` and `convT7`) is 2 for the first stage of CVA-MVSNet and $(1, 2, 2)$ for stages 2 and 3 because of the reduced number of depth planes. For the same reason, the output padding P (cf. `convT7`) is 1 for stage 1 and $(0, 1, 1)$ for stages 2 and 3. The cost volume (`aggregated cost volume`) has 32 channels for stage 1, 16 channels for stage 2, and 8 channels for stage 3.

Layer	**input**	**k**	**s**	**p**	**op**	**chns**	**bn**	**act**
`conv0`	`aggregated cost volume`	3	1	1		$(32, 16, 8) \rightarrow 8$	✓	ReLU
`conv1`	`conv0`	3	2	1		$8 \rightarrow 16$	✓	ReLU
`conv2`	`conv1`	3	1	1		$16 \rightarrow 16$	✓	ReLU
`conv3`	`conv2`	3	2	1		$16 \rightarrow 32$	✓	ReLU
`conv4`	`conv3`	3	1	1		$32 \rightarrow 32$	✓	ReLU
`conv5`	`conv4`	3	S	1		$32 \rightarrow 64$	✓	ReLU
`conv6`	`conv5`	3	1	1		$64 \rightarrow 64$	✓	ReLU
`convT7`	`conv6`	3	S	1	P	$64 \rightarrow 32$	✓	ReLU
`convT8`	`conv4` + `convT7`	3	2	1	1	$32 \rightarrow 16$	✓	ReLU
`convT9`	`conv2` + `convT8`	3	2	1	1	$16 \rightarrow 8$	✓	ReLU
`prob`	`conv0` + `convT9`	3	1	1		$8 \rightarrow 1$		$\mathrm{Softmax}_{\mathrm{depth}}$

network is called for each new keyframe. It would be possible to estimate depth only for every second keyframe to trade-off runtime and reconstruction quality.

Combining all the aforementioned measures decreases the inference time from 158 ms to 25.6 ms, a 83.2% decrease, while maintaining reasonable reconstruction quality and without optimizations like Nvidia TensorRT. Additionally, the network could be used on every second keyframe, i.e. with ca. 2 Hz. This combination makes our CVA-MVSNet $20\times$ real-time on an RTX 2080 super. The embedded Nvidia Jetson AGX Xavier has ca. 15% of the computing power of the RTX 2080 super and thus our CVA-MVSNet could potentially reach real-time on this device even without NVIDIA TensorRT. The classic SLAM components of TANDEM can be run in real-time on an embedded device [74], hence the proposed TANDEM could likely be implemented on an embedded device in real-time while maintaining reasonable reconstruction quality.

Table 10: Hyperparameter Table.

	Value	Description
`min depth`	0.01	Minimal depth value in meters used for generating the depth planes for our CVA-MVSNet.
`max depth`	10.0	Maximal depth value in meters used for generating the depth planes for our CVA-MVSNet.
`depth planes`	$(48, 4, 4)$	Number of depth planes for each stage.
`depth intervals`	$(0.213, 0.106, 0.053)$	The distance in meters between two depth planes for each stage. For the first stage, the planes are evenly spaced between the minimum and maximum depth. For stages 2 and 3 the interval is divided by 2 and 4, respectively.
optimizer	Adam	We use the default parameters: $(\beta_1, \beta_2) = (0.9, 0.999)$ and $\epsilon = 10^{-8}$.
learning rate	0.004	Learning rate at the start of the schedule.
learning rate schedule	linear decay	Linear decay from `lr` to $\texttt{lr}/100$.
epochs	50	The number of training epochs on the Replica dataset.
batch size	4×2	We train with 4 GPUs with batch size 2 on each GPU without synchronized batch norm.
BN momentum	0.1	Batch normalization momentum.
image size	640×480	The size of images and depth maps on the finest scale, i.e. stage three.

Table 11: Timing results for TANDEM on EuRoC/V101. We show the averaged per-frame times and the averaged per-keyframe times and timed 2685 single frames for which 722 keyframes were created. Processing one frame takes 47 ms, which gives a throughput of ca. 21 FPS. The CVA-MVSNet, TSDF fusion, and Bundle Adjustment are run only for keyframes and thus we show the time taken per keyframe as well as the average time taken per frame, which is ca. four times lower due to the ratio of frames and keyframes. Note that the CVA-MVSNet per-keyframe time is lower than what we reported in the main paper (cf. Table 1) because we use asynchronicity and parallelism between CPU and GPU to ensure real-time performance.

	Per Frame [ms]	**Per Keyframe [ms]**
Number	2685	722
CVA-MVSNet	22.6	53.0
TSDF Fusion		29.3
Coarse Tracking	10.5	
Bundle Adjustment	13.9	45.2
Sum	47.0	

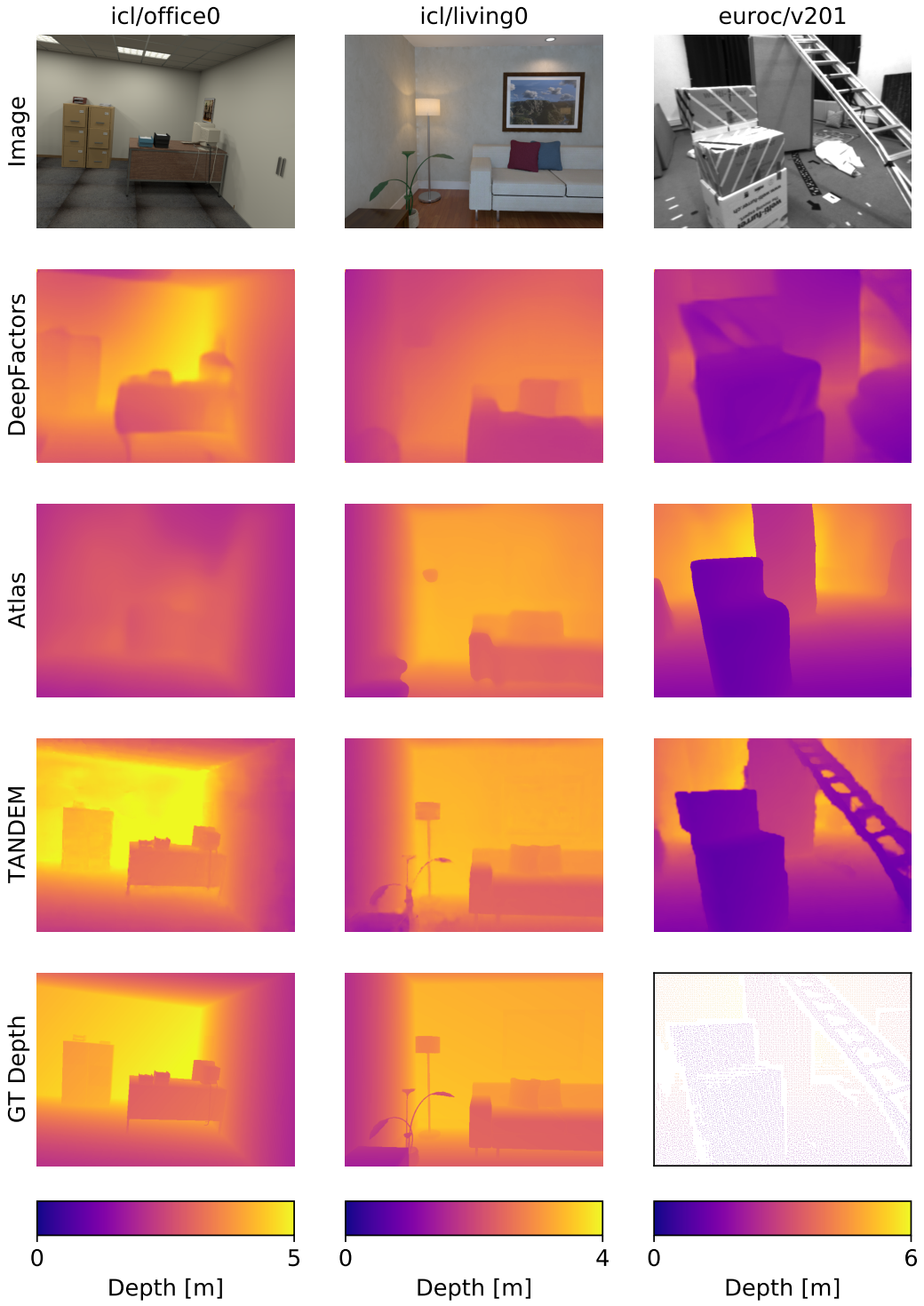

Figure 7: Depth comparison for DeepFactors [7], Atlas [9], and TANDEM on unseen sequences. TANDEM produces finer-scale details, e.g. the plant in the second column, or the ladder in the third column. For EuRoC only sparse ground-truth depth is available. This is a high-resolution version of Figure 3 from the main paper. In Figure 8 we show further qualitative results.

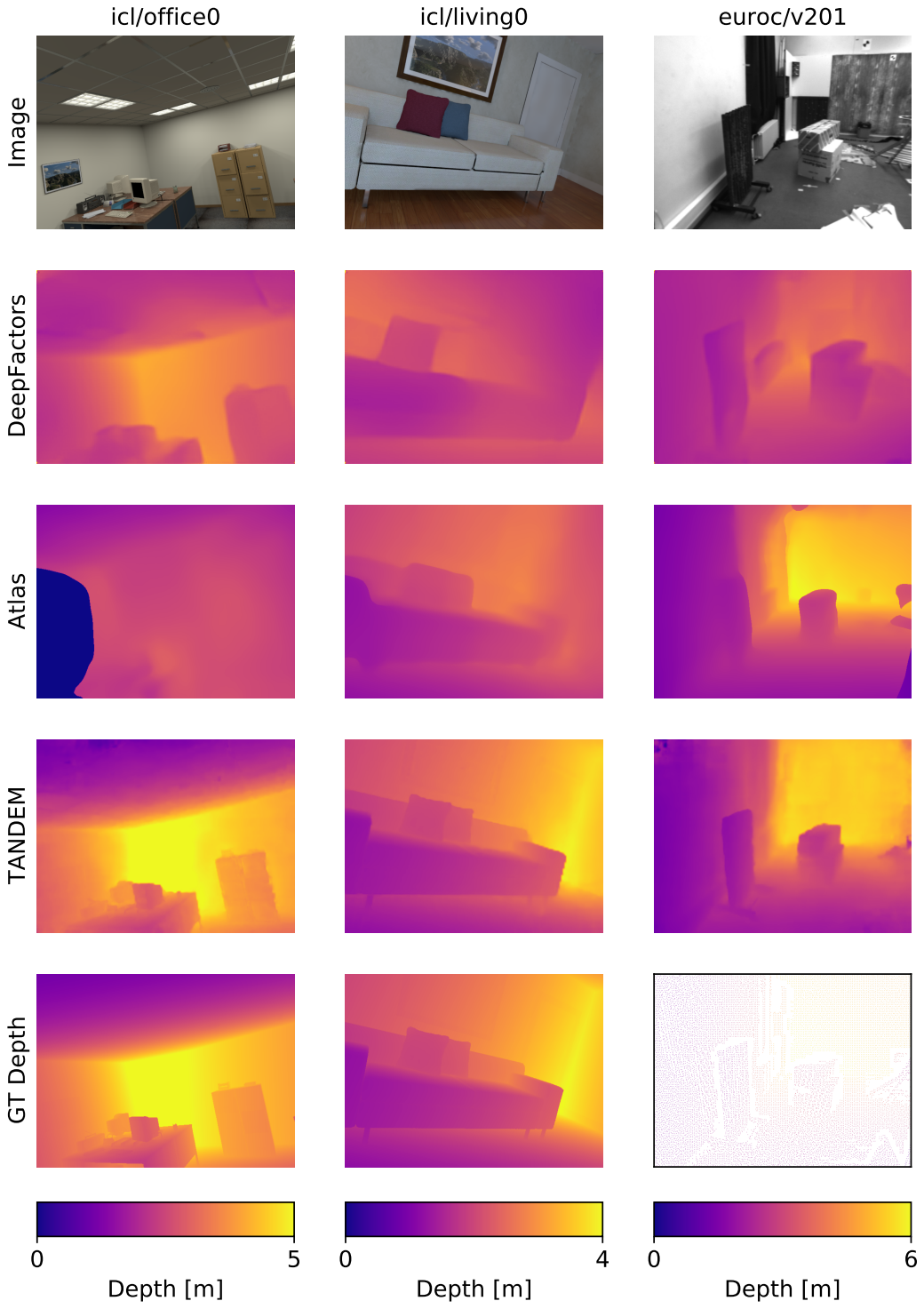

Figure 8: Further depth comparison for DeepFactors [7], Atlas [9], and TANDEM on unseen sequences. TANDEM produces finer-scale details, e.g. the computers in the first column, the pillows in the second column, or the radiator in the third column. However, TANDEM can produce outliers due to the cost volume-based formulation (cf. third column upper left corner of the image). For Atlas, the reconstruction of office0 is too small and thus the rendered depth has an invalid region (the blue blob in bottom left). For EuRoC only sparse ground-truth depth is available.

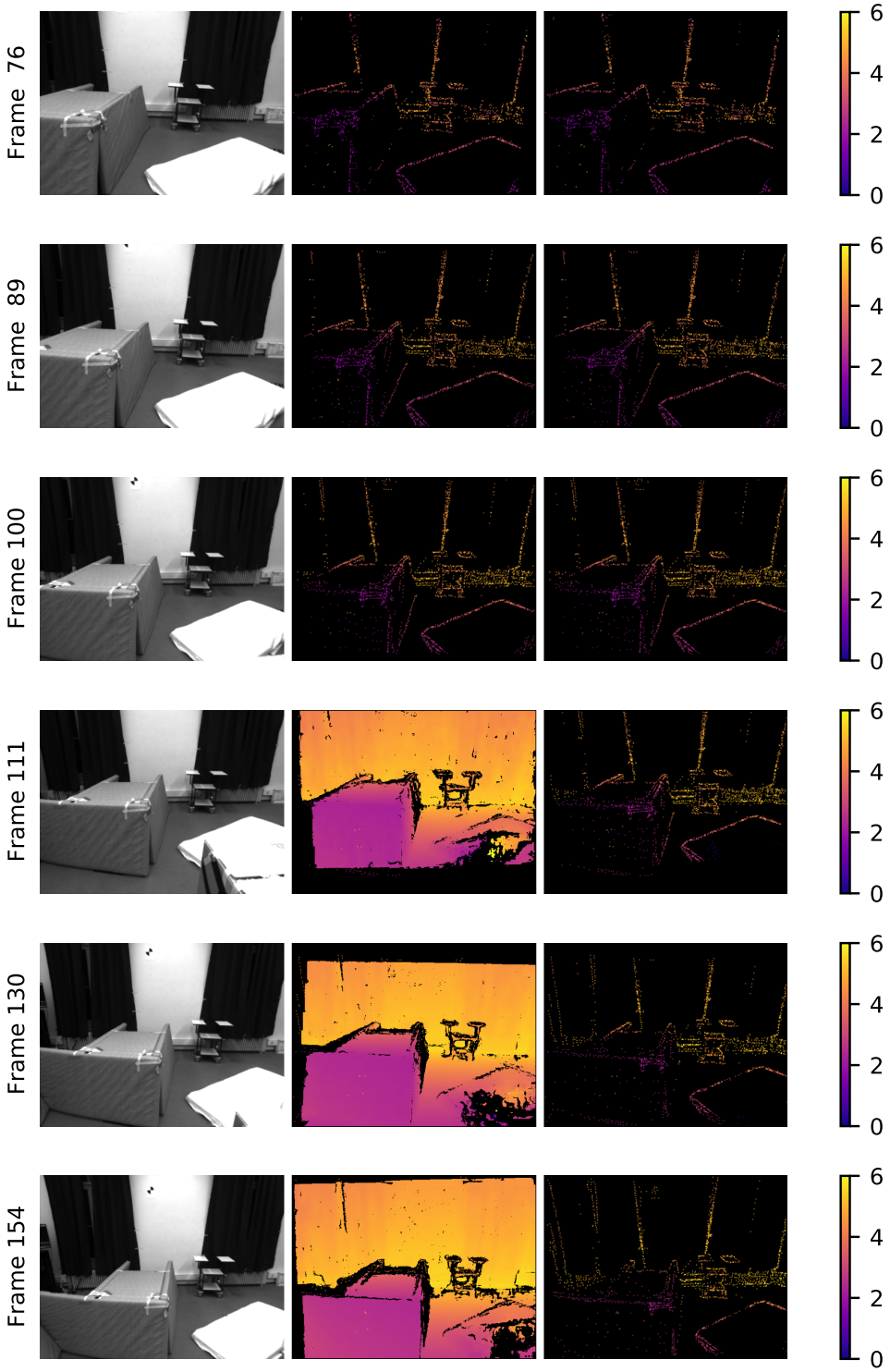

Figure 9: Tracking Depth Maps for EuRoC/V201. For every second keyframe we show the image (*left*), the depth map used for tracking by TANDEM (*middle*), and the sparse depth map that would be used without the dense tracking (*right*). For the first few keyframes no dense depth is available and thus TANDEM uses the sparse depth map for tracking. Note that, as in DSO, the sparse depth maps are slightly dilated before they are used for tracking. Further frames are shown in Figure 10.

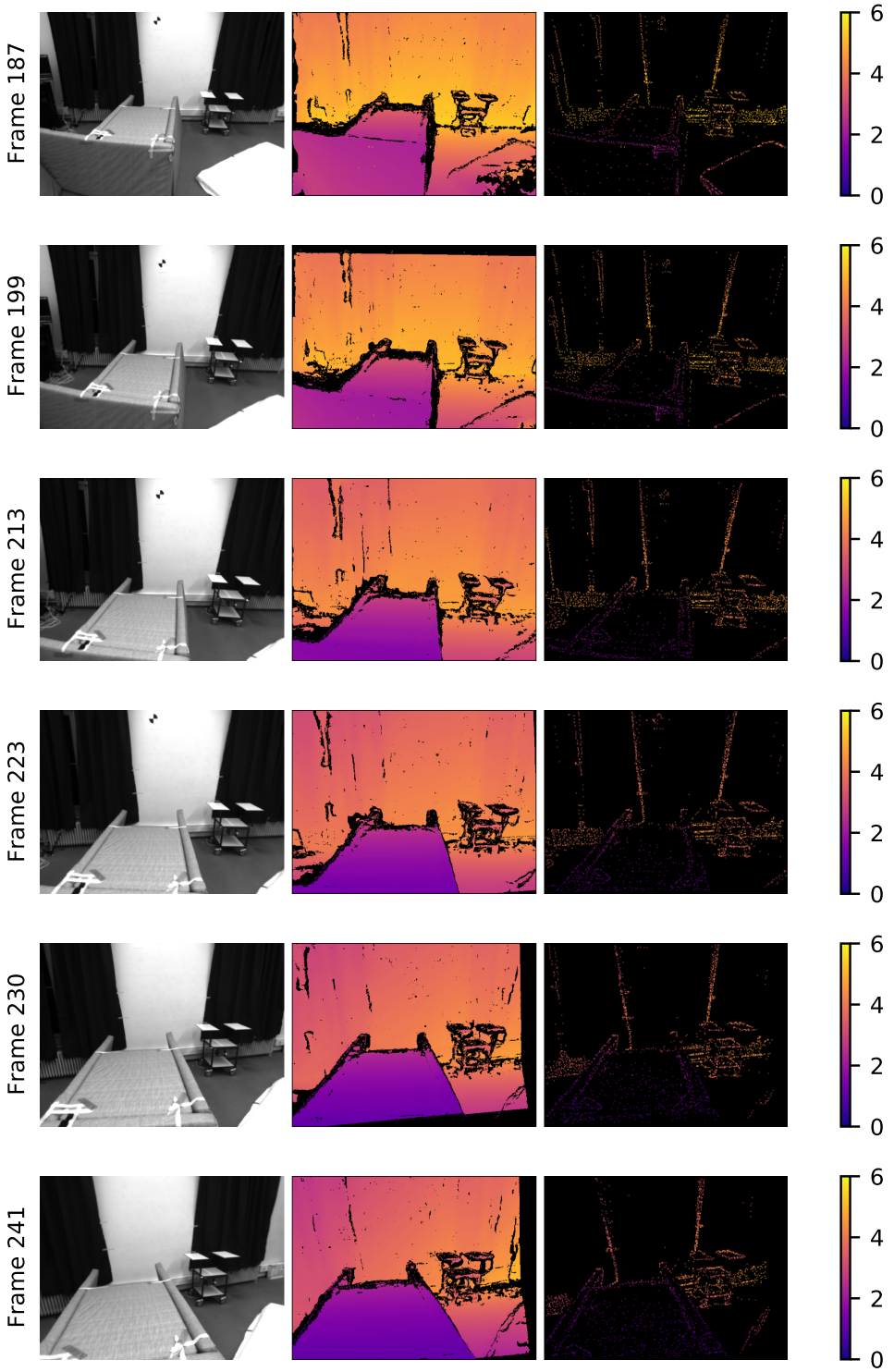

Figure 10: Tracking Depth Maps for EuRoC/V201. For every second keyframe we show the image (*left*), the depth map used for tracking by TANDEM (*middle*), and the sparse depth map that would be used without the dense tracking (*right*). The nearly dense depth map represents the scene well and thus the dense tracking can give more accurate results than the sparse tracking [67, 57]. The dense depth map also incorporates the sparse depth values which can be seen at occlusion boundaries. Note that, as in DSO, the sparse depth maps are slightly dilated. Previous frames are shown in Figure 9.